Journal of
Materials Chemistry A

Accepted Manuscript

This article can be cited before page numbers have been issued, to do this please use: C. Bi, Y. Shao, Y. Yuan, Z. Xiao, C. Wang, Y. Gao and J. Huang, *J. Mater. Chem. A*, 2014, DOI: 10.1039/C4TA04007D.

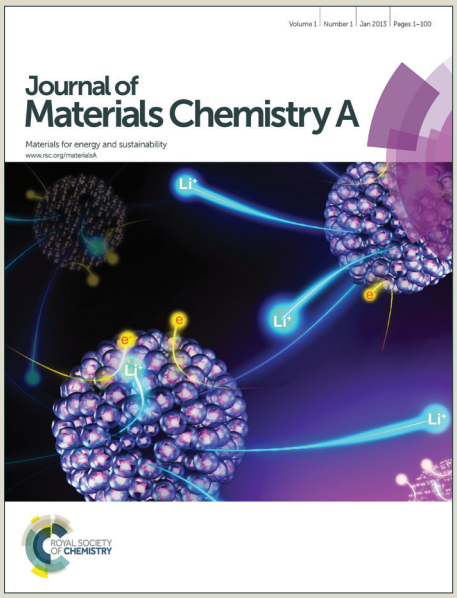

ROYAL SOCIETY OF CHEMISTRY

www.rsc.org/materialsA

Dynamic Article Links ►
View Article Online
DOI: 10.1039/C4TA04007D

Cite this: DOI: 10.1039/c0xx00000x

www.rsc.org/xxxxxx

PAPER

Understanding the Formation and Evolution of Interdiffusion Grown Organolead Halide Perovskite Thin Films by Thermal Annealing

Cheng Bi,[a] Yuchuan Shao,[a] Yongbo Yuan,[a] Zhengguo Xiao,[a] Chenggong Wang,[b] Yongli Gao,[b] and Jinsong Huang*[a]

Received (in XXX, XXX) Xth XXXXXXXXX 20XX, Accepted Xth XXXXXXXXX 20XX
DOI: 10.1039/b000000x

Organolead trihalide perovskites are emerging excellent active materials for thin film solar cells. Here, the formation and evolution of methylammonium lead iodide perovskite thin films grown by the low-temperature thermal annealing induced interdiffusion process is investigated. It is found that thermal annealing not only drives the formation of perovskite but also affects the morphology, optoelectronic properties and correlated device performance. The thermal annealing at 105 °C quickly drives the formation of phase-pure perovskite in a short time of 15 min, and followed thermal annealing up to two hours continuously increases perovskite crystallinity and grain size without losing film continuity or coverage. The measured Hall mobility increases monotonically to 36.0 cm^2 V^{-1} s^{-1} upon annealing, which is correlated with the increased crystallinity and grain size. Device efficiencies increase with improved short circuit current density and fill factor under longer annealing time up to two hours, and the highest device efficiency of 13.4% is achieved. It is found that the reduction of work function in the perovskite films, caused by increased annealing duration, is linearly correlated with the open circuit voltage loss, which points out a path for the further increase of the device efficiency.

1. Introduction

Solar energy is a reliable, renewable and clean resource in contrast to conventional fossil fuels. Thin film photovoltaics, with features like low cost, light weight, easy fabrication, are promising for solar energy harvesting.[1-3] One effective way to reduce the cost of photovoltaic devices is to increase their efficiencies.[3] Thermal annealing is broadly applied in both organic and inorganic thin film solar cells to improve device performance.[4-11] In organic solar cell, thermal annealing was often used to increase the crystallinity of polymers and to form the optimized polymer/fullerene domain sizes for charge generation in polymer solar cells.[4,6,12-14] In inorganic thin film solar cells, thermal annealing treatment governs the performance of devices by playing versatile functions, such as facilitating the incorporation of alkali into polycrystalline Cu(In, Ga)Se_2 (CIGS) thin film for defect passivation,[10,15,16] increasing crystallinity,[17,18] coarsening the crystalline domains,[11,19] and homogenizing crystal structure in CIGS active layer.[9,20]

Recently, organolead halide perovskites are emerging as a new generation of photovoltaic materials for both sensitized solid-state mesoporous structure solar cells and thin film solar cells.[1,21-32] The materials are inexpensive, nature-abundant and solution processable. Efficiency above 15% was achieved by perovskite-based devices with both planar and mesoporous structure after few years of development.[21,23-25,31,32] Mesoporous structure which usually applies TiO_2 as electron conductive layer requires high-temperature sintering process, and photocatalytic TiO_2 raises the risk of deteriorating device stability under UV light.[33] Recent demonstration of a low temperature solution-processed TiO_2-free hybrid solar cell employing perovskite/fullerene bilayer structure as the active layer, provides a possibility to produce perovskite photovoltaic devices by using the recently developed large scale, high throughput solution deposition methods for polymer solar cell.[34,35] However the poor perovskite film quality with very rough and non-continuous perovskites leads to low device efficiency due to the quick crystallization of perovskite from the blended precursor solution.[27] It has been recently realized by the community that there is a strong correlation between the perovskite film quality and the device performances. In one of our recent studies,[36] spin coating lead iodine (PbI_2) and methylammonium iodide (MAI) stacked layers was found to form continuous and pin-hole free perovskite films, as illustrated in Figure 1. It was found the thermal annealing right after the spin coating of the stacked layers was critical to improve the device efficiency. One can speculate that the thermal annealing here has two different functions that is different from regular thermal annealing processes: 1) driving the interdiffusion of PbI_2 and MAI precursor for the formation of the perovskite, and 2) inducing the recrystallization and grain growth in the formed perovskite films. In this manuscript, we report the thermal annealing effect on structural, electrical, optical properties of methylammonium lead iodide ($MAPbI_3$) perovskite thin films and correlated device performance. We observed

View Article Online
DOI: 10.1039/C4TA04007D

strong influence of thermal annealing on crystallinity, grain size of the perovskite films as well as the carrier mobility and concentration, correlating well with the device performance.

2. Experimental Section

MAI synthesis: MAI was synthesized by the method reported elsewhere.[37] Typically, hydroiodic acid (HI) (15.0 mL, 57 wt% in water, Alfa Aesar) solution was mixed with methylamine (MA) (13.5 mL, 40 wt% in aqueous solution, Alfa Aesar) in an ice bath with stirring for 2 h under the nitrogen atmosphere. The resulting solution was evaporated by a rotary evaporator to remove the solvent. The MAI was precipitated during evaporation process and was purified by washing it three times with diethyl ether. After that, the obtained powder was dried in vacuum.

Film formation and device fabrication: The PbI_2 and MAI were dissolved in anhydrous dimethylformamide (DMF) and 2-propanol with a concentration of 400 mg ml^{-1} and 40 mg ml^{-1}, respectively. To produce high performance device, a relative high concentration of MAI solution was used here. Before the device fabrication, the indium tin oxide (ITO) glass substrates have been cleaned by water, acetone and isopropyl alcohol (IPA). After that, poly(3,4-ethylenedioxythiophene)poly(styrenesulfonate) (PEDOT:PSS) was spin coated on the substrate at a rotation speed of 3000 rpm for 60 s. The 25 nm thick PEDOT film was thermally annealed at 135 °C for 20 mins. Hot PbI_2 precursor solution (70 °C) was spin coated on the PEDOT:PSS surface in nitrogen at a rotation speed of 6000 rpm for 45 s, and then the PbI_2 film was dried at 70 °C for 15 mins. The MAI solution (room temperature) was spin coated on the top of PbI_2 film at a rotation speed of 6000 rpm for 35 s. The spin coated MAI layer was dried at 75 °C for 10 mins. It's known that high annealing temperature of above 150 °C can cause quick decomposition of the formed perovskite films (Figure S1).[28,38] In our study, in order to avoid significant decomposition, the as-fabricated films were annealed in nitrogen at a relatively low temperature of 105 °C with varied annealing time from 15 mins to 3 hrs.

In order to reduce the surface defects of the perovskite film an additional phenyl-C61-butyric acid methyl ester (PCBM) film was spin coated on top of the formed perovskite layer from a 20 mg ml^{-1} PCBM solution in dichlorobenzene (DCB), as described elsewhere.[36] After that, 20 nm C_{60}, 7 nm 2,9-dimethyl-4,7-diphenyl-1,10-phenanthroline (BCP) and 100 nm aluminium layer was sequentially deposited onto the film by thermal evaporation. The resulted devices have a structure of ITO/ PEDOT:PSS (25 nm)/$MAPbI_3$ (280 nm)/PCBM (20 nm)/C_{60} (20 nm)/BCP (8 nm)/Al (100 nm). The working area of these devices is 6 mm^2.

Film characterization: The single path absorption spectra of the perovskite film were measured by Evolution 201 UV-Visible spectrometer (thermo Scientific). X-ray diffraction (XRD) patterns of the film were obtained by a Rigaku D/Max-B X-ray diffractometer with Bragg-Brentano parafocusing geometry. A Co-Kα tube was employed in XRD measurement with a working wavelength of 1.79 Å. The morphology of the film was studied by Quanta 200 FEG Environmental Scanning Electron Microscope (SEM). Hall Effect and conductivity measurements were conducted in air by using six contacts Hall bar method, during which the DC current flowing through the perovskite film was applied by Keithley Model 2400 and the Hall voltage was recorded by Keithley Model 4200. The validity of the measurement was verified by measuring a standard *n*-type Si sample with a doping level of 1.8×10^{14} cm^{-3}. The work function of the perovskite films was measured by ultraviolet photoelectron spectroscopy (UPS), which was performed in a VG ESCA Lab system equipped with an ultrahigh vacuum system and a He discharge lamp. The UPS spectra were recorded using unfiltered He I (21.2 eV) excitation source, and the samples were biased at -5.0 V to observe the low-energy secondary cutoff. The UV light spot size on the sample was about 1 mm in diameter.

Device characterization: Xenon-lamp-based solar simulator (Oriel 67005, 150 W Solar Simulator) was used to provide simulated AM 1.5G irradiation (100 mW/cm^2). The light intensity was calibrated by a KG5 colour-filtered Si diode (Hamamatsu S1133). Keithley Model 2400 was used for the current-voltage measurement. The series resistance was obtained by fitting the current density-voltage (*J-V*) curves in the bias range of 1.3-1.5 V, and the shunt resistance was obtained by fitting the *J-V* curves at bias range of -0.2-0.2 V.

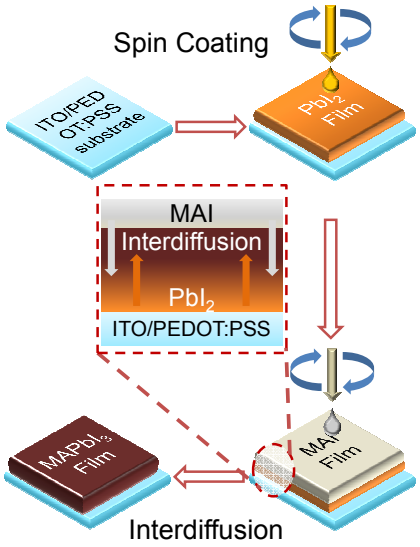

Figure 1. Schematic illustration of the fabrication procedure of interdiffusion grown perovskite film: interdiffusion process on the two of stacked precursor layers starts after deposition and reaches completeness during further thermal annealing.

3. Result and Discussion

3.1. Ultraviolet-Visible Absorption Study

In order to understand the formation and evolution process of $MAPbI_3$ film during thermal annealing processes, the optical properties of the fabricated films was firstly studied. As shown in Figure 2, the film dried at 75 °C for 15 mins has broad absorption with absorption edge around 800 nm, confirming the formation of $MAPbI_3$ right after drying. The absorption in long wavelength range around 600-800 nm increased gradually in the first hour of annealing, which indicates that the reaction between precursors was not completed right after drying, and a thermal annealing is required to drive the interdiffusion of MAI and PbI_2 precursors

View Article Online
DOI: 10.1039/C4TA04007D

into each other. The absorption remains unchanged after one hour of annealing.

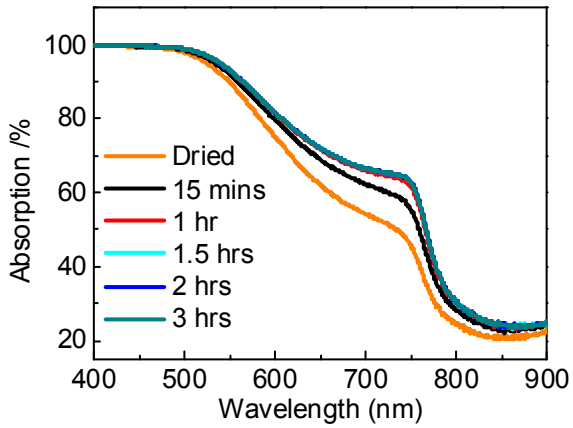

Figure 2. Single path absorption spectra of $MAPbI_3$ perovskite films dried at 75 °C for 10 mins and annealed at 105 °C for varied durations.

3.2. X-Ray Diffraction Study

In order to understand the formation and evolution of perovskite films' phase and crystallization by thermal annealing, XRD measurement of the films has been carried out. Figure 3(a) shows the XRD patterns of the annealed films with different annealing time. The peaks origin from MAI (23.13°) and PbI_2 (14.96°) phase disappeared after the first 15 mins of thermal annealing at 105 °C, confirming the quick reaction between the MAI and PbI_2 under thermal annealing. The XRD peaks observed in 16.69°, 23.50°, 33.40° and 37.45° are assigned to (110), (112), (220) and (310) crystal planes of the $MAPbI_3$ perovskite structure, which agrees with previous studies using Cu-Kα radiation source.[23,28,39] No peak from impurity phase was observed after 15mins of thermal annealing, indicating the formation of perovskite phase under 105 °C is efficient. After 3 hrs of thermal annealing, small amount of PbI_2 phase showed up, which should origin from the decomposition of perovskite after long time annealing. All the annealed films have similar XRD patterns while the diffraction peaks become sharper with the increased annealing time. As illustrated in Figure 3(b), the full width at half maximum (FWHM) of the (110) peak reduce gradually from 0.226° to 0.150° when thermal annealing time increased from 15 mins to 3 hrs. It should be noted that both increased crystallinity with less defects and larger grain size with less grain boundaries can result in a sharper XRD peak. The increased crystalline grain size with thermal annealing was confirmed by the following SEM characterization. Also, the Hall effect and UPS measurement showed a decreased hole concentration with increased annealing time, which indicates a reduced doping effect caused by the defects because point defects in $MAPbI_3$ work as dopants rather than generating trap states in the bandgap.[40,41] Thus, the sharper peak observed here should result from both enlarged grain size and increased crystallinity. In addition, it is observed that the intensity of (110) diffraction peak at 16.69° increased gradually in the first 1.5 hrs of annealing, and then kept almost the same in the following 1.5 hrs, as shown in Figure 3(c). Meanwhile, the relative intensity of (110) diffraction peak to the (310) diffraction peak does not change significantly during thermal annealing, as shown in Figure 3(c). Thus the increased (110) peak intensity should be caused by increased crystallinity rather than crystal orientation change.

3.3. Scanning Electron Microscopy Study

The increase of grain size in perovskite films upon thermal annealing was confirmed by the SEM study. The SEM images in Figure 4 (a-b) show the overall film morphology of the perovskite films after thermal annealing of 15 mins or 3 hrs, respectively. The perovskite films grown on ITO/PEDOT: PSS by interdiffusion method were continuous and compact even after 3 hrs of thermal annealing, which is in contrast to the discontinuous films fabricated from pre-mixed precursors.[27] Figure 4 (c-g) show the morphology change of the perovskite film during thermal annealing. The grain size distribution derived from these images is shown in Figure 4 (h). The average grain size increased with the thermal annealing, consisting with the gradually decreased FWHM of XRD peaks in Figure 3(b). After 15 mins of thermal annealing the average gain size was 190 nm, and then it increased to around 350 nm and 380 nm after 2 hrs and 3 hrs annealing, respectively. The maximum grain size was 600-700 nm. It is noticed that the grain size is comparable with or larger than the thickness of the film so that there is minimized grain boundary in the charge collection direction of the annealed perovskite films, which contributes to the high efficiency in the perovskite solar cells.

3.4. Hall Effect Measurement

In order to study the influence of thermal annealing on the carrier

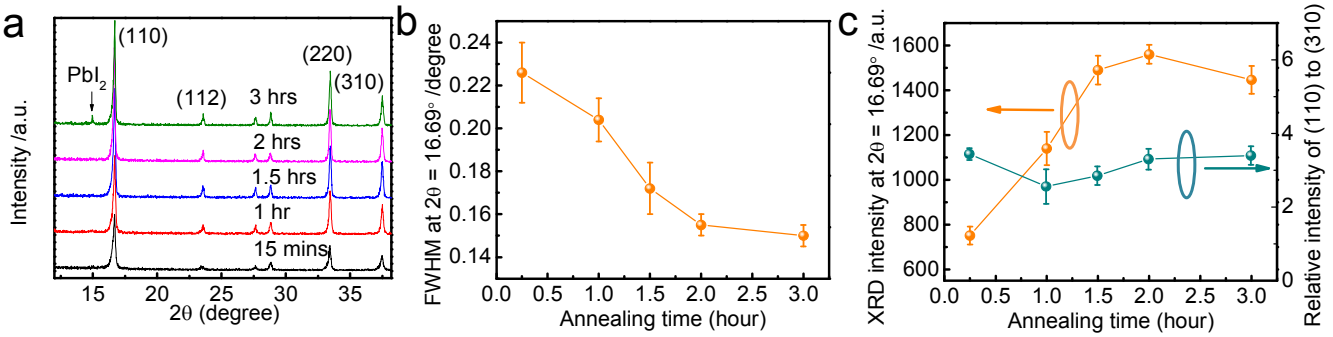

Figure 3. (a) XRD patterns of $MAPbI_3$ perovskite films annealed at 105 °C for varied durations; (b) Evolution of film's FWHM of (110) diffraction peak with increased annealing time; (c) Variation of XRD peak intensity at 2θ=16.69° (left Y-axis) and its relative intensity to (310) peak (right Y-axis) with increased annealing time.

View Article Online
DOI: 10.1039/C4TA04007D

concentration and carrier mobility of the perovskite film, we conducted Hall effect measurement. The perovskite's electronic

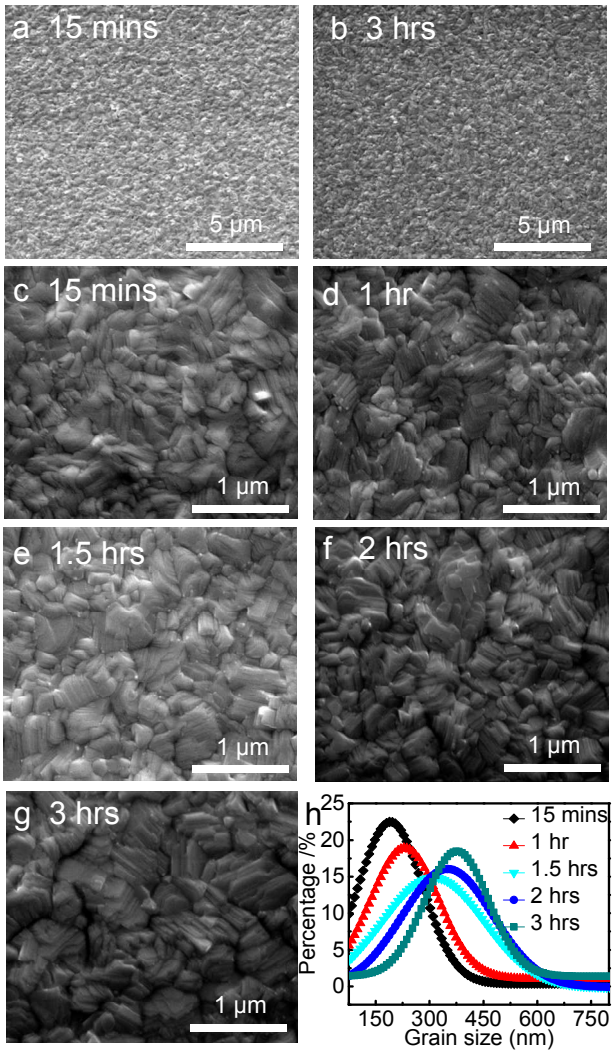

Figure 4.(a-b) Morphology of $MAPbI_3$ perovksite films annealed at 105 °C for (a) 15 mins, and (b) 3 hrs; (c-g) Enlarged SEM images of $MAPbI_3$ films with different annealing times: (c) 15 mins, (d) 1 hr, (e) 1.5 hrs, (f) 2 hrs, and (g) 3 hrs; (h) Grain size distribution of the films with varied annealing duration.

property is sensitive to the fabrication methods. All the films grown by interdiffusion method showed *p*-type behaviour which is in contrast to the *n*-type perovskite formed from pre-mixed perovskite precursor.[42,43] Recently calculation results on atomic defects in perovskites showed that Pb and MA vacancy acts as *p*-type dopant and I vacancy act as *n*-type dopant.[40,41] In the interdiffusion-grown perovskite films, a fixed amount of PbI_2 layer was prepared (150 nm), and then a relatively high concentration precursor solution (40 mg ml^{-1}) was used to deposit a MAI layer on the top of PbI_2 layer,[44] which most likely resulted in point defects like Pb vacancies during interdiffusion process and thus resulted in *p*-type perovskite films. Figure 5 shows the variation of hole concentration and hole mobility with annealing time. There is a clear increase of Hall mobility from 13.7 $cm^2 V^{-1} s^{-1}$ to 28.7 $cm^2 V^{-1} s^{-1}$, accompanied with a reduction of hole concentration from 5.9×10^{14} cm^{-3} to 2.7×10^{14} cm^{-3}, for films with

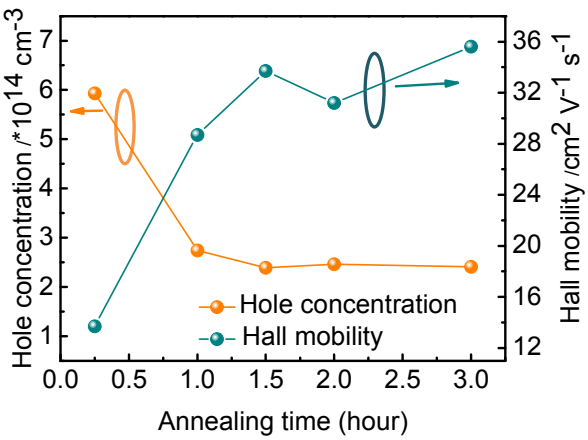

Figure 5. Carrier concentration and Hall mobility of the perovskite films with varied annealing durations.

increased annealing time from 15 mins to 1 hr. It again indicates the formation of stoichiometric, phase pure, perovskite. The Hall mobility further increases from 28.7 $cm^2 V^{-1} s^{-1}$ to 36.0 $cm^2 V^{-1} s^{-1}$, accompanied by the slight reduction of hole concentration from 2.7×10^{14} cm^{-3} to 2.4×10^{14} cm^{-3} with continued thermal annealing up to 3 hrs. This increased mobility correlates well with increased grain crystallinity and grain size in the perovskite films revealed by XRD and SEM measurements. The reduced hole concentration can be explained by fewer defects such as atomic vacancies, interstitial atoms or grain boundaries which can be a source of excess carriers. It is interesting that the PbI_2 from slight decomposition at the third hour did not increase the hole concentration. This may result from the small amount of PbI_2 in grain boundaries which did not work as dopant and was less likely to cause defects since PbI_2 has a larger bandgap (2.3 eV).[45]

3.5. Device's Photovoltaic Performance

The larger grains reduced the total grain boundary area, which is expected to reduce the charge recombination at the grain boundaries and improve device performance. The interdiffusion grown perovskite films with proper thermal annealing possess desired features for perovskite thin film photovoltaic application, including full coverage on substrates, complete conversion of precursors, improved crystallinity and enlarged grain size. To investigate the annealing effect on the device performance, we fabricated devices with structure of ITO/PEDOT: PSS (25 nm)/$MAPbI_3$ (280 nm)/PCBM (20 nm)/C_{60} (20 nm)/BCP (8 nm)/aluminium (100 nm). Here, the PCBM/C_{60} bilayer was applied on the top of the annealed perovskite film to passivate the surface defects on the perovskite film, which was found critical in achieving high efficiency devices.[33,36,43] Figure 6(a) compares the *J-V* curves of the perovskite devices with different thermal annealing time at a temperature of 105 °C. The short-circuit current density (J_{SC}), open-circuit voltage (V_{OC}) and fill factor (FF) derived from *J-V* curves were summarized in Figure 6(b). The J_{SC} increased from 14.9 mA cm^{-2} to 19.0 mA cm^{-2} after 2 hrs of thermal annealing. The FF also increased steadily from 69% to

View Article Online
DOI: 10.1039/C4TA04007D

78% after 2 hrs of thermal annealing and did not decrease in the following annealing process. The maximum PCE of 13.4% was

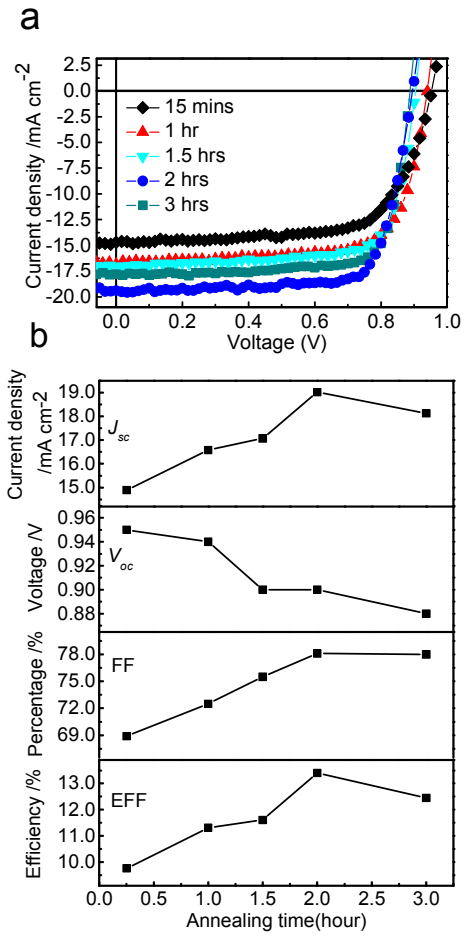

Figure 6. Performance of the $MAPbI_3$ perovskite devices made of films after 105 °C annealing for different durations: (a) Photocurrent density-voltage curves of the devices under simulated AM 1.5 irradiation (100 mW cm^{-2}); (b) Variation on devices' parameters, J_{SC}, V_{OC}, FF and PCE, with increased annealing durations.

obtained by annealing the perovskite films at 105 °C for 2 hrs due to the significantly increased FF and J_{SC}. The much increased FF and J_{SC} can be explained by the reduction of bulk trap density and increased carrier mobility, which origin from the increased perovskite stoichiometry, crystallinity and grain size. It's worth to notice that the obtained perovskite device has a FF as large as 78%, which is larger than that of most perovskite photovoltaic devices with planar heterojunction or mesoporous structure had FF of 60% - 75%.[1, 1-26] In addition, the shunt resistance increased from 1.51×10^4 ohm to over 3.71×10^4 ohm with longer annealing time, as shown in Table 1. This should be attributed to the reduced carrier concentration, which gives a lower leakage in devices. Also, reduced series resistances were observed, which should come from increased carrier mobility, improved interface and better crystallinity with fewer defects.

Nevertheless, the thermal annealing on interdiffusion grown perovskite film led to a reduced V_{OC}, as shown in Figure 6 (b).

Table 1. Shunt and series resistances of the devices with perovskite films annealed after varied duration

Annealing Time (hr)	0.25	1	1.5	2	3
Series resistances (ohm cm^2)	5.46	3.49	1.67	1.78	1.43
Shunt resistances ($\times10^4$ ohm)	1.51	1.68	2.57	3.83	3.71

Three hours of annealing pulled down the V_{OC} from 0.95 V to 0.88 V. Generally, an increased grain size leads to larger V_{OC} because of the reduced charge recombination at grain boundaries, while the increased grain size with annealing time observed in this work ruled out the grain boundary recombination as the dominating factor for the reduced V_{OC}. We noticed that the hole concentration was reduced with thermal annealing. This reduction of carrier concentration has a negative impact to V_{OC}. The V_{OC} of photovoltaic device is ultimately determined by the quasi-Fermi energy level splitting of the electrons and holes under illumination:

$$V_{OC} = k_B T \ln \frac{(p+\Delta p)(n+\Delta n)}{n_i^2} \quad (1)$$

where k_B, T, p, n, Δp, Δn, n_i^2 are Boltzmann constant, temperature, hole concentration in dark, electron concentration in dark, photogenerated hole concentration, electron concentration and intrinsic carrier concentration, respectively. Since our materials are p-type ($p>>n$), and photons generated equal number of electrons and holes, the equation (1) can be simplified as:

$$V_{OC} = k_B T \ln \frac{(p+\Delta p)\Delta p}{n_i^2} \quad (2)$$

where Δp is a constant that is determined by the incident light intensity and by assuming the charge generation efficiency is same for all the films. Therefore a smaller hole concentration gives a reduced V_{OC} as is the case for perovskite solar cells reported here.

The reduced hole concentration in annealed perovskite films is also confirmed by the UPS study. The work function of the annealed perovskite films gradually reduced from 5.21 eV to 5.08 eV with increased annealing time. It should be noted the work function of the perovskite films formed by interdiffusion is much different from those formed from premixed precursors.[46] A reduced work function lifts the Fermi energy toward the middle of the bandgap, yielding a smaller hole concentration as measured, as shown in Figure 7(a). It shows that annealing is a method to control work function and even doping concentration in interdiffusion-grown perovskite films. Since hole concentration is exponentially dependent on both the shift of Fermi energy level and the V_{OC}, it is expected that there is a linear relationship between the work function and V_{OC}. Figure 7(b) shows the plot of V_{OC} and work function on the same figure with shifted V_{OC}. A clear linear correlation between them was observed for the devices with annealing time less than two hours. The discrepancy for the three hour annealing sample might be caused by the decomposition of the perovskite films, yielding a larger V_{OC} than that predicted from Fermi energy shift. The

View Article Online
DOI: 10.1039/C4TA04007D

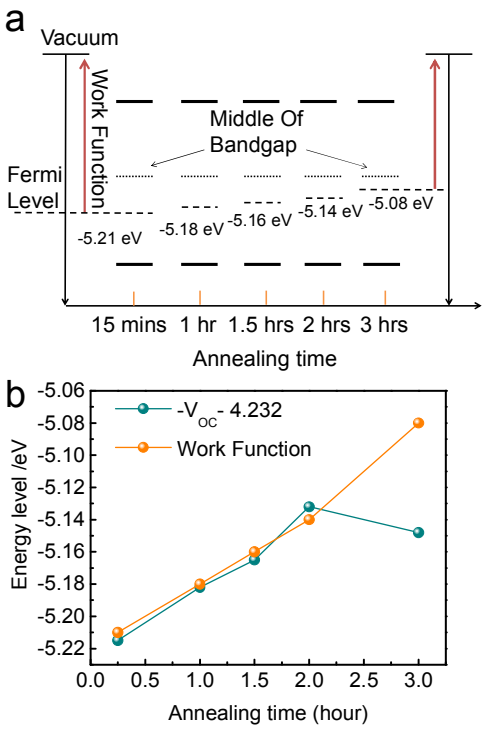

Figure 7. (a) Energy diagram of Fermi energy shifting during thermal annealing; (b) $MAPbI_3$ perovskite films' work function and V_{OC} of the corresponding devices with increased annealing durations.

results shown here point out a future direction to increase the device efficiency is to slightly increase the carrier concentration of the perovskite layer without causing significant charge recombination.

4. Conclusion

Interdiffusion method for fabricating perovskite solar cell provides a low cost and feasible solution to achieve high performance due to the formation of continuous absorber films with full surface coverage. By understanding thermal annealing effect on perovskite films, we demonstrated the crystallinity and grain size is critical to optimize the device performance. Increased annealing time at relatively low temperature (105 °C) overall improved device performance by increasing J_{SC} and *FF*. The highest PCE of 13.4% was achieved when perovskite absorber layer was treated by 2 hrs of thermal annealing at 105 °C. In addition, it is expected that annealing process can optimize the performance of perovskite solar cells with mesoporous architecture or formed from blending precursors.

Notes and references

[a] *Department of Mechanical and Materials Engineering and Nebraska Center for Materials and Nanoscience, University of Nebraska-Lincoln, Lincoln, Nebraska 68588-0656, USA;*
[b] *Department of Physics and Astronomy, University of Rochester, Rochester, NY 14627, USA;*
* *To whom correspondence should be addressed-mail: jhuang2@unl.edu*

† Electronic Supplementary Information (ESI) available [XRD pattern for 150°C annealing]. See DOI: 10.1039/b000000x/

1. P. Docampo, J. M. Ball, M. Darwich, G. E. Eperon, H. J. Snaith, *Nat. Commun.*, 2013, **4**, 2761.
2. C. H. Lee, D. R. Kim, I. S. Cho, N. William, Q. Wang, X. Zheng, *Sci. Rep.*, 2012, **2**, 1000.
3. V. Shrotriya, *Nat. Photonics.*, 2009, **3**, 447-449.
4. W. Ma, C. Yang, X. Gong, K. Lee, A. J. Heeger, *Adv. Funct. Mater.,* 2005, **15**, 1617-1622.
5. J. A. Mikroyannidis, A. N. Kabanakis, S. S. Sharma, G. D. Sharma, *Adv. Funct. Mater.,* 2011, **21**, 746-755.
6. F. Liu, Y. Gu, J. W. Jung, W. H. Jo, T. P. Russell, *J. Polym. Sci., Part B: Polym. Phys.,* 2012, **50**, 1018-1044.
7. J. Jo, S.-S. Kim, S.-I. Na, B.-K. Yu, D.-Y. Kim, *Adv. Funct. Mater.,* 2009, **19**, 866-874.
8. T. M. Clarke, A. M. Ballantyne, J. Nelson, D. D. C. Bradley, J. R. Durrant, *Adv. Funct. Mater.,* 2008, **18**, 4029-4035.
9. M.-G. Tsai, H.-T. Tung, I.-G. Chen, C.-C. Chen, Y.-F. Wu, X. Qi, Y. Hwu, C.-Y. Lin, P.-H. Wu, C.-W. Cheng, *J. Am. Ceram. Soc.,* 2013, **96**, 2419-2423.
10. S. Niki, M. Contreras, I. Repins, M. Powalla, K. Kushiya, S. Ishizuka, K. Matsubara, *Prog. Photovolt. Res. Appl.*, 2010, **18**, 453-466.
11. C.-J. Hsu, H.-S. Duan, W. Yang, H. Zhou, Y. Yang, *Adv. Energy. Mater*., 2013, **4**, 1301287
12. S. Engmann, C. R. Singh, V. Turkovic, H. Hoppe, G. Gobsch, *Adv. Energy. Mater*., 2013, **3**, 1463-1472.
13. F. Padinger, R. S. Rittberger, N. S. Sariciftci, *Adv. Funct. Mater*., 2003, **13**, 85-88.
14. C. J. Brabec, S. Gowrisanker, J. J. M. Halls, D. Laird, S. Jia, S. P. Williams, *Adv. Mater.* 2010, **22**, 3839-3856.
15. M. Bodeg Ård, K. Granath, L. Stolt, *Thin Solid Films*, 2000, **361–362**, 9-16.
16. L. Kronik, D. Cahen, H. W. Schock, *Adv. Mater.,* 1998, **10**, 31-36.
17. M. Venkatachalam, M. D. Kannan, S. Jayakumar, R. Balasundaraprabhu, N. Muthukumarasamy, *Thin Solid Films*, 2008, **516**, 6848-6852.
18. M. Krunks, O. Kijatkina, H. Rebane, I. Oja, V. Mikli, A. Mere, *Thin Solid Films,* 2002, **403–404**, 71-75.
19. M. Kaelin, D. Rudmann, F. Kurdesau, T. Meyer, H. Zogg, A. N. Tiwari, *Thin Solid Films,* 2003, **431–432**, 58-62.
20. B. Bob, B. Lei, C.-H. Chung, W. Yang, W.-C. Hsu, H.-S. Duan, W. W.-J. Hou, S.-H. Li, Y. Yang, *Adv. Energy. Mater*., 2012, **2**, 504-522.
21. K. Wojciechowski, M. Saliba, T. Leijtens, A. Abate, H. J. Snaith, *Energy Environ. Sci*., 2014, **7**, 1142-1147.
22. H.-S. Kim, C.-R. Lee, J.-H. Im, K.-B. Lee, T. Moehl, A. Marchioro, S.-J. Moon, R. Humphry-Baker, J.-H. Yum, J. E. Moser, M. Gratzel, N.-G. Park, *Sci. Rep.*, 2012, **2**, 591.
23. J. Burschka, N. Pellet, S.-J. Moon, R. Humphry-Baker, P. Gao, M. K. Nazeeruddin, M. Gratzel, *Nature*, 2013, **499**, 316-319.
24. D. Liu, T. L. Kelly, *Nat. Photonics.*, 2014, **8**, 133-138.
25. M. Liu, M. B. Johnston, H. J. Snaith, *Nature*, 2013, **501**, 395-398.
26. O. Malinkiewicz, A. Yella, Y. H. Lee, G. M. Espallargas, M. Graetzel, M. K. Nazeeruddin, H. J. Bolink, *Nat. Photonics.*, 2014, **8**, 128-132.

View Article Online
DOI: 10.1039/C4TA04007D

27. G. E. Eperon, V. M. Burlakov, P. Docampo, A. Goriely, H. J. Snaith, *Adv. Funct. Mater.*, 2014, **24**, 151-157.
28. A. Dualeh, N. Tétreault, T. Moehl, P. Gao, M. K. Nazeeruddin, M. Grätzel, *Adv. Funct. Mater.*, 2014, **24**, 3250-3258.
29. S. D. Stranks, G. E. Eperon, G. Grancini, C. Menelaou, M. J. P. Alcocer, T. Leijtens, L. M. Herz, A. Petrozza, H. J. Snaith, *Science*, 2013, **342**, 341-344.
30. Q. Chen, H. Zhou, Z. Hong, S. Luo, H.-S. Duan, H.-H. Wang, Y. Liu, G. Li, Y. Yang, *J. Am. Chem. Soc.*, 2014, **136**, 622-625.
31. N. J. Jeon, J. H. Noh, Y. C. Kim, W. S. Yang, S. Ryu, S. I. Seok, *Nat. Mater.*, 2014, **13**, 897-903.
32. H. Zhou, Q. Chen, G. Li, S. Luo, T.-B. Song, H.-S. Duan, Z. Hong, J. You, Y. Liu, Y. Yang, *Science*, 2014, **345**, 542-546.
33. T. Leijtens, G. E. Eperon, S. Pathak, A. Abate, M. M. Lee, H. J. Snaith, *Nat.Commun.*, 2013, **4**, 2885.
34. J.-Y. Jeng, Y.-F. Chiang, M.-H. Lee, S.-R. Peng, T.-F. Guo, P. Chen, T.-C. Wen, *Adv. Mater.*, 2013, **25**, 3727-3732.
35. J. You, Z. Hong, Y.(Michael) Yang, Q. Chen, M. Cai, T.-B. Song, C.-C. Chen, S. Lu, Y. Liu, H. Zhou, Y. Yang, *ACS Nano*, 2014, **8**, 1674-1678.
36. Z. Xiao, C. Bi, Y. Shao, Q. Dong, Y. Yuan, C. Wang, Y. Gao, J. Huang, *Energy. Environ. Sci.*, 2014, **7**, 2619-2623.
37. M. M. Lee, J. Teuscher, T. Miyasaka, T. N. Murakami, H. J. Snaith, *Science*, 2012, **338**, 643-647.
38. Q. Chen, H. Zhou, T.-B. Song, S. Luo, Z. Hong, H.-S. Duan, L. Dou, Y. Liu, and Y. Yang, *Nano Lett.*, 2014, **14**, 4158-4163.
39. Y. Zhao, K. Zhu, *J. Phys. Chem. Lett.*, 2013, **4**, 2880-2884.
40. W.-J. Yin, T. Shi, Y. Yan, *Appl. Phys. Lett*., 2014, **104**, 063903.
41. J. Kim, S.-H. Lee, J. H. Lee, K.-H. Hong, *J. Phys. Chem. Lett*., 2014, **5**, 1312-1317.
42. B. Conings, L. Baeten, C. De Dobbelaere, J. D'Haen, J. Manca, H.-G. Boyen, *Adv. Mater.*, 2014, **26**, 2041-2046.
43. Q. Wang, Q. Dong, Z. Xiao, Y. Yuan, J. Huang, *Energy Environ. Sci.*, 2014, **7**, 2359-2365.
44. Q. Wang, Y. Shao, H. Xie, L. Lyu, X. Liu, Y. Gao, J. Huang, *Appl. Phys. Lett*., 2014, *submitted*.
45. Q. Chen, H. Zhou, T.-B. Song, S. Luo, Z. Hong, H.-S. Duan, L. Dou, Y. Liu, Y. Yang, *Nano Lett.,* 2014, **14**, 4158−4163.
46. P. Schulz, E. Edri, S. Kirmayer, G. Hodes, D. Cahen, A. Kahn, *Energy Environ. Sci.*, 2014, **7**, 1377-1381.